Computers in Biology and Medicine 114 (2019) 103435

Contents lists available at ScienceDirect

Computers in Biology and Medicine

journal homepage: http://www.elsevier.com/locate/compbiomed

Assessing the accuracy of computer-planned osteotomy guided by stereolithographic template: A methodological framework applied to the mandibular bone harvesting

Alessandro Cristoforetti [a,b], Luca De Stavola [c], Andrea Fincato [c], Michela Masè [b,d], Flavia Ravelli [b], Giandomenico Nollo [a,d,*], Francesco Tessarolo [a,d]

[a] Department of Industrial Engineering, University of Trento, Via Sommarive, 9, 38123, Trento, Italy
[b] Department of Physics, University of Trento, Via Sommarive, 14, 38123, Trento, Italy
[c] Department of Neurosciences, School of Dentistry, University of Padua, Via Giustiniani, 5, 35128, Padua, Italy
[d] IRCS-HTA, Bruno Kessler Foundation – FBK, Via Sommarive, 18, 38123, Trento, Italy

ARTICLE INFO

Keywords:
3D computer-guided surgery
Osteotomy
Lithographic surgical guide
Dental implants
Bone harvesting
Image segmentation
Image registration
Accuracy assessment

ABSTRACT

Intraoral autologous bone grafting represents a preferential choice for alveolar reconstruction prior to dental implant placement. Bone block harvesting guided by a computer-planned lithographic template is a novel and promising technique for optimizing the volume of harvested material, while controlling the osteotomy 3D position with respect to delicate anatomical structures. We provide a quantitative framework to non-invasively estimate the accuracy of this technique. In the proposed framework, the planned osteotomy geometry was compared to the real outcome of the procedure, obtained by segmentation of post-procedural cone beam computed tomography data. The comparison required the rigid registration between pre and post-procedural mandibular models, which was automatically accomplished by minimizing the sum of squared distances via a stochastic multi-trial iterative closest point algorithm. Bone harvesting accuracy was quantified by calculating a set of angular and displacement errors between the planned and real planes which characterized the excision block. The application of the framework to four cases showed its capability to quantify the tolerance associated with computer-guided bone harvesting techniques with submillimetric accuracy (<0.4 mm), within the limits of native image resolution. The validation methodology proved suitable for defining the safety margins of osteotomy surgical planning.

1. Introduction

The functional and aesthetic success of prosthodontic restorations in presence of atrophy of the alveolar crest is highly dependent on bone augmentation procedures [1,2], which allow implant placement in the optimal position. Autologous bone grafting is currently considered the "gold standard" among different bone reconstruction techniques, as it offers higher bone survival rate and implant success, thanks to the non-immunogenic, osteo-inductive and osteo-conductive properties of the augmentation material [3–6]. Intraoral donor sites are particularly advantageous in terms of accessibility and proximity to recipient sites, morbidity, operative time, and costs [7]. In fact, bone harvesting in the retromolar region of the mandibular ramus has proved to be an effective and safe method to treat up to medium-size alveolar defects [8].

In spite of the benefits, intraoral sites may offer a limited available bone volume and may be associated with post-procedural complications, including mandibular and neurologic damage, which can affect patient acceptance in the long term [2,9–11]. The use of high-resolution cone beam computed tomography (CBCT) has introduced key advantages in implant dentistry [12], allowing a pre-procedural 3D planning of the intervention. Although pre-procedural imaging can also inform the harvesting procedure, the intra-procedural use of this anatomical information is limited due to the lack of reference points for accurately identifying the position of the mandibular canal, mental nerve, and dental roots. Conservative cutting of the cortical plate in the ramus apical portion is the current strategy to contain the risk of nerve damage [9,13], while damage to other anatomical structures cannot be fully avoided due to the limited control on freehand incisions. On the other

* Corresponding author. Department of Industrial Engineering, University of Trento, via Sommarive, 9, 38123, Trento, Italy.
E-mail address: giandomenico.nollo@unitn.it (G. Nollo).

https://doi.org/10.1016/j.compbiomed.2019.103435
Received 10 July 2019; Received in revised form 4 September 2019; Accepted 4 September 2019
Available online 5 September 2019

hand, computer-guided implant surgery is becoming increasingly popular in dental rehabilitation, even if evidence of a clear superiority with respect to conventional methods is still inconclusive [14,15]. In particular, an established static computer-assisted procedure consists in the preoperative virtual planning of a template fitted to the local anatomy, the stereolithographic printing of the template, and its use during the intervention as a guide for drilling and implant insertion. Computer-designed stereolithographic surgical guides may offer an advantage with respect to freehand methods once the surgeon is aware of the possible accuracy deviations [16–21].

Drawing from this technology, an analogous approach has been recently investigated for guiding the intraoral harvesting of autologous bone [22–24]. Applying this novel technique, the surgeon can take full advantage of pre-procedural, CBCT based, surgical planning using a stereolithographic template, which is fitted to the harvesting site cortical bone and guides the movement of the cutting tool. This allows to control the position, angulation and depth of osteotomy lines, maximizing the volume of the harvestable bone block at minimal risk of damage for nearby delicate anatomical structures. Given their recent introduction, computer-guided stereolithographic bone block harvesting systems still lack a proper accuracy evaluation to define their safety and precision with respect to other harvesting techniques. In this paper we propose a framework for estimating the accuracy of these novel systems, which systematically quantifies the discrepancy between the planned and real harvesting procedures in terms of positional and angular deviations of the osteotomy planes. The framework was preliminarily tested on a limited number of cases to assess the feasibility and the suitability of the method, with the ultimate goal to use it for validating the harvesting technique on a wider cohort of patients.

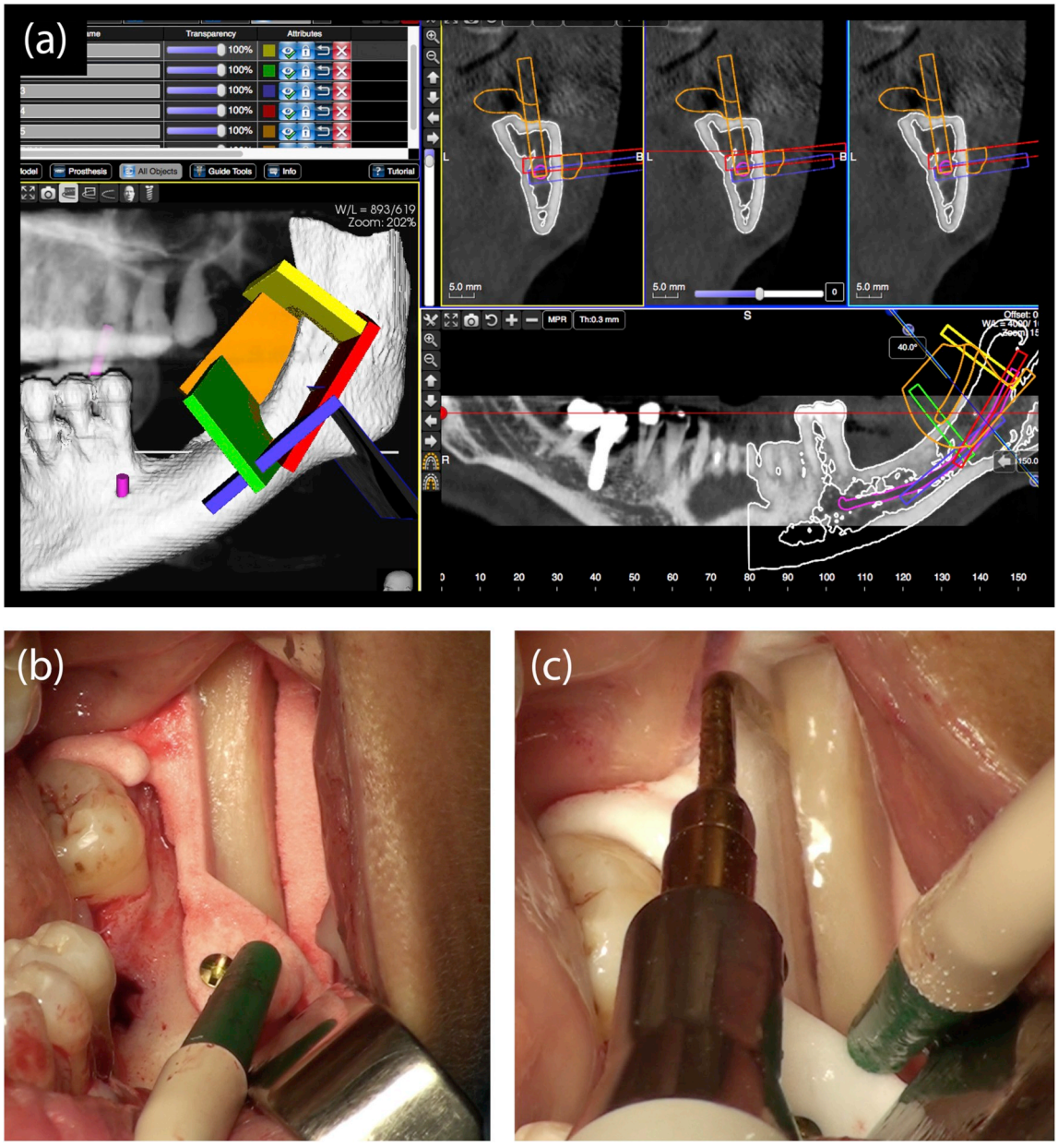

Fig. 1. Example of computer-guided bone block harvesting. (a) Virtual planning and construction of the surgical guide model. Five incision planes were defined, one distal (yellow), one mesial (green), one cranial (orange), and two apical (red and purple) (b) Lithographic surgical guide screwed in situ. (c) Piezoelectric scalpel performing the osteotomy directed by the internal faces of the surgical guide. (For interpretation of the references to color in this figure legend, the reader is referred to the Web version of this article.)

2. Methods

2.1. Materials

2.1.1. Dataset

The validation method was tested on four cases, two obtained from a human cadaver head (case 1 and 2), and two from anonymized images of two patients (case 3 and 4) who underwent autogenous bone grafting for the application of dental implants [24]. The use of medical images abided by the local statutory requirements. The validation used both the pre-procedural tomographic dataset, acquired for virtual planning and production of the surgical guides, and the follow-up post-procedural dataset acquired after the surgical procedure. The cadaveric imaging dataset was produced by veterinary CT scanner Vimago™ (Epica Medical Innovations, San Clemente CA, USA) with isotropic image reconstruction at 0.4 mm, while the in vivo datasets were obtained by CBCT scanner (VGi Evo, NewTom, Imola, Italy) with isotropic image reconstruction at 0.3 mm. The virtual guide model and its incision planes were exported from the planning software in STL format. All the algorithms necessary for the validation were developed as in-house built software, using Matlab programming platform (MathWorks, Inc., Natick, Massachusetts, USA).

2.1.2. Bone grafting procedure

The harvesting and grafting procedure was previously described in detail [23,24]. Briefly, the surgical planning was performed using diagnostic and analytic software (3Diagnosys 4.0, 3DIEMME, Cantù CO, Italy), to obtain cross-sectional images and 3D reconstructions (Fig. 1(a)). The mandible area most suited for bone harvesting was identified based on the visualization of the mental nerve and foramina, the alveolar canal, and the dental roots, while a safety margin from these anatomic structures was kept in setting the position of the cutting planes. The shape of the bone block to be removed was approximately rectangular with a cranial, an apical, and two lateral (mesial and distal) sides. The virtual surgical guide had the internal faces defined by the projections of the cutting planes outside the bone surface, and was shaped in computer-aided design (CAD) software (PlastyCAD, 3DIEMME, Cantù CO, Italy) in order to fit the local anatomy. A computer-assisted manufacturing (CAM) process (3Dfast, Padua, Italy) was used to build the guide in medical polyamide. The surgical procedure was performed under general sedation and local anesthesia. After the guide was anchored and screwed on the donor site (Fig. 1(b)), the osteotomy cuts were made leaning the piezoelectric scalpel on the internal faces of the surgical guide (Fig. 1(c)). The surgical guide unambiguously directed the outline of the incision, while its depth was implicitly determined by the analysis of the volumetric image. After bone removal, the harvesting site was filled with collagen sponge and the bone block was grafted following a previously described bone augmentation approach [25].

2.2. Validation procedure

The framework of the validation process is summarized in the flowchart of Fig. 2. The procedure consisted of the following steps. 1) Segmentation of the cortical bone containing the osteotomy (mandible) from the pre and post-procedural datasets. A model including softer (cancellous) bone is also segmented in the post-procedural dataset, suitable to detect the performed incisions. 2) Registration of the cortical bone mandibular models in order to correctly align the pre-procedural planned incision planes in the post-procedural dataset. 3) Segmentation of the real incision surfaces from the post-procedural soft mandibular model as sets of samples, and fitting of a spatial reference frame specific for each incision. 4) Quantification of several displacement and angular discrepancy components between the planned and real incision surfaces according to the reference frame.

2.2.1. Model segmentation

In the pre-procedural CBCT/CT images the mandibular cortical bone was segmented by applying a manual intensity threshold [26] set case by case according to visual inspection by the physician, ranging from 1000 to 1200 grey level values in our dataset. Separation from contiguous bone structures was obtained by connected component analysis [27], aided by manual selection whenever necessary. Major image artefacts were also manually removed. The segmentation produced a full mandible mesh model $\mathcal{M}_{pre}$. An equivalent anatomy was segmented also from the post-procedural CBCT/CT using the same threshold, producing the mesh model $\mathcal{M}_{post}$ and the binary mask B_{post}, which represented the internal volume of $\mathcal{M}_{post}$. It was unnecessary to exclude from the mandibular models the harvesting region, since the registration algorithm had the capability to automatically detect major dissimilarities between the models via a cutoff threshold. A mandibular mesh model $\mathcal{M}_{soft}$, inclusive of less dense bone tissue, was similarly produced from post-procedural images by lowering the intensity threshold to 600–800 grey level values. The model $\mathcal{M}_{soft}$ was more suitable for the delineation

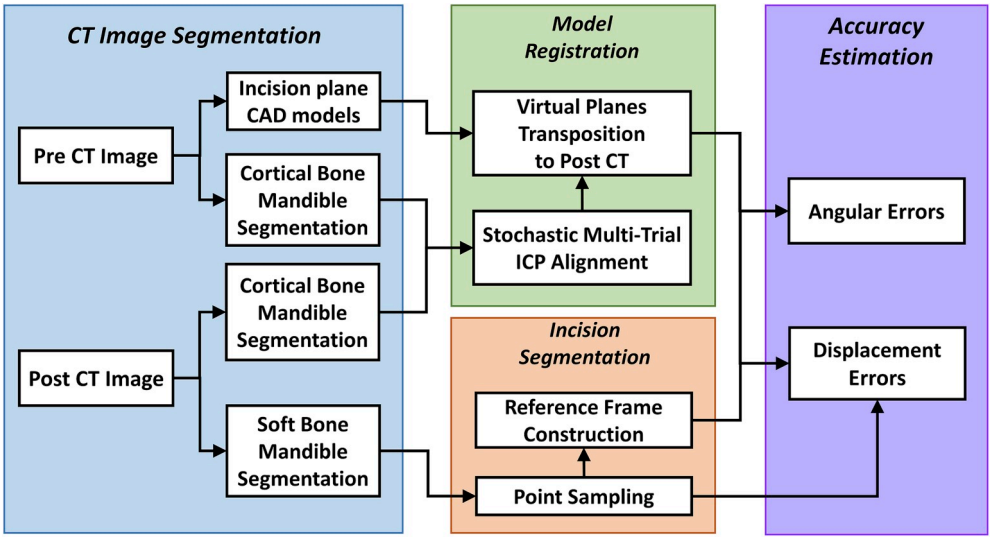

Fig. 2. Flowchart of the validation process for computer-guided bone grafting. CT = computed tomography; CAD = computer-aided design; ICP = iterative closest point.

of the incision surface exposed by the surgical excision.

2.2.2. Model registration

The registration of the pre-procedural mandibular model $\mathscr{M}_{pre}$ to the post-procedural model $\mathscr{M}_{post}$ was regarded as a surface rigid alignment problem [28], and solved by minimizing a target function G composed of the root mean square of distances from $\mathscr{M}_{pre}$ to $\mathscr{M}_{post}$. The registration was composed of two phases: the global phase, where the search range was wide and only a sparse subset of N points on $\mathscr{M}_{pre}$ was used, and the refinement phase, where the range was narrower, a denser set of points was employed, and a cutoff threshold of 2 mm was imposed on distances to exclude grossly mismatching parts [29]. Each registration phase was based on a stochastic multi-trial approach, adapted from Refs. [30,31]. Specifically, a set of 20 repeated alignment trials were performed with the initial position of $\mathscr{M}_{pre}$ perturbed by random displacements and rotations, and the trial result with minimal G was kept as solution. The minimization of the target function G in each trial was accomplished by an iterative closest point (ICP) algorithm [32,33], summarized below.

In the ICP algorithm, the set of N points $\{\mathbf{p}_i\}$ sampled on $\mathscr{M}_{pre}$ was iteratively matched to the closest points $\{\mathbf{q}_i\}$ on the surface of $\mathscr{M}_{post}$ and rigidly transformed by $\mathbf{T}$:

$$\mathbf{T}(\mathbf{p}_i) = \mathbf{R}\mathbf{p}_i + \mathbf{t}, \tag{1}$$

where $\mathbf{R}$ is a rotation matrix and $\mathbf{t}$ is a translation vector. At each iteration the transformation $\mathbf{T}$ was determined by least square minimization of the residual distances between the transformed points and their closest pairs [34], i.e. by minimization of the target function:

$$G(\mathbf{T}) = \frac{1}{N}\sqrt{\sum_{i=1}^{N} \mathbf{T}(\mathbf{p}_i) - \mathbf{q}_i^2}. \tag{2}$$

This orthogonal Procrustes problem was solved by singular value decomposition (SVD) [35]. Briefly, if P and Q are matrices of the demeaned row vectors $\{\mathbf{p}_i\}$ and $\{\mathbf{q}_i\}$:

$$P = \left[\mathbf{p}_1^T, \ldots, \mathbf{p}_N^T\right] - \overline{\mathbf{p}}^T,\ \overline{\mathbf{p}} = \frac{1}{N}\sum_{i=1}^{N} \mathbf{p}_i, \tag{3a}$$

$$Q = \left[\mathbf{q}_1^T, \ldots, \mathbf{q}_N^T\right] - \overline{\mathbf{q}}^T,\ \overline{\mathbf{q}} = \frac{1}{N}\sum_{i=1}^{N} \mathbf{q}_i, \tag{3b}$$

and V and U are produced by SVD of PQ^T:

$$PQ^T = U\Sigma V^T, \tag{4}$$

then the rotation matrix is given by Refs. [36,37]:

$$\mathbf{R} = V\Delta U^T,\ \Delta = diag\left(1, 1, det\left(VU^T\right)\right), \tag{5}$$

where *diag* defines a diagonal matrix and *det* indicates the determinant.

The translation vector was thus obtained by:

$$\mathbf{t} = \overline{\mathbf{q}} - \mathbf{R}\overline{\mathbf{p}}. \tag{6}$$

The ICP algorithm was halted when reaching a maximum number of iterations (200), or when the decrement of G in 10 iterations was inferior to a predefined threshold (0.01 mm). The net transformation applied to the samples $\{\mathbf{p}_i\}$ was finally extended to the whole $\mathscr{M}_{pre}$ model.

The N points $\{\mathbf{p}_i\}$ used in the ICP trials were subsampled on $\mathscr{M}_{pre}$ surface with a minimal distance threshold of 2 mm in the global phase, while in the refinement phase the threshold was set to 0.3 mm, i.e. the CBCT/CT data resolution. The initial perturbation range was 20 mm for displacement and 30 deg for rotation angles in the global phase, and 2 mm and 3 deg in the refinement phase.

The identification of the closest points between the models during each iteration was the most computationally expensive part of the algorithm. The computational burden was reduced by obtaining the closest point information from an Euclidean distance transform [38], precomputed on the binary mask B_{post}. The distance image D was signed, and contained the distance of each voxel from the B_{post} mask boundary, with negative values indicating voxels inside the mask. The three coordinates of the closest points were also stored in three separate matrices: Q_x, Q_y, and Q_z. At each ICP iteration, the distance of points $\{\mathbf{p}_i\}$ from $\mathscr{M}_{post}$ was quickly obtained by linear interpolation of D at $\{\mathbf{p}_i\}$ positions, while the coordinates of the closest points $\{\mathbf{q}_i\}$ were similarly computed by interpolation of Q_x, Q_y, and Q_z.

The registration results were assessed by visual inspection and the analysis of several quality parameters, i.e. the root mean square (RMS), median, and 90 percentile of the final residual distances under the cutoff threshold of 2 mm. The percentage of $\mathscr{M}_{pre}$ mesh nodes under the cutoff was also reported.

The rigid transformation applied to $\mathscr{M}_{pre}$ was finally used to align the model of the planned surgical guide and its incision planes to the reference frame of the post-procedural data.

2.2.3. Incision surface segmentation

The incision surfaces exposed by the bone harvesting procedure were detected on the post-procedural soft bone model $\mathscr{M}_{soft}$ by manually selecting N_s samples $\{\mathbf{s}_i\}_{i=1\ldots N}$ for each incision, as shown in Fig. 3(a). The samples were arranged in three rows: two delineating the inner and outer rims of the incision, and one placed in the middle. Inter-sample distance in a row was at least 0.5 mm.

The N_s samples $\{\mathbf{s}_i\}$ on each incision surface identified the effective incision plane. This plane was fitted to $\{\mathbf{s}_i\}$ by singular value decomposition (SVD) of the demeaned sample coordinate matrix, identifying three principal axes (Fig. 3(b)):

- The binormal axis $\hat{\mathbf{b}}$, which was perpendicular to the plane and corresponded to the smallest singular value. Its direction pointed toward the part of tissue removed.
- The normal axis $\hat{\mathbf{n}}$, corresponding to the middle singular value, lay on the plane and was perpendicular to the incision direction (movement of the scalpel). Its direction pointed outward of the bone.
- The tangent axis $\hat{\mathbf{t}}$, corresponding to the largest singular value, lay on the plane and was parallel to the incision direction. Its direction was defined by the cross product of the binormal and normal axes.

The segmentation of each effective incision plane defined thus the reference frame ($\hat{\mathbf{b}}$, $\hat{\mathbf{n}}$, $\hat{\mathbf{t}}$), with origin set to the barycenter of the N_s samples:

$$\overline{\mathbf{s}} = \frac{1}{N_s}\sum_{i=1}^{N_s} \mathbf{s}_i. \tag{7}$$

2.2.4. Incision accuracy estimation

The planned incision plane was identified by the binormal axis $\hat{\mathbf{b}}^*$, whose direction was chosen coherent with $\hat{\mathbf{b}}$ (toward the part of tissue removed), and by the plane distance b^* from the origin $\overline{\mathbf{s}}$, so that $b^*\hat{\mathbf{b}}^*$ was the closest point of the plane to $\overline{\mathbf{s}}$. The accuracy estimation consisted in computing the angular discrepancy between the planned and effective incision planes, separated into rotation components around normal and tangent axes, as shown in Fig. 3(c), and the displacement discrepancy of the effective incision samples from the planned plane.

The angular errors informed about inclination differences between the effective ($\hat{\mathbf{b}}$) and planned ($\hat{\mathbf{b}}^*$) binormals, and were defined according to:

- *Total inclination error*:

$$\theta_{tot} = arccos(\hat{\mathbf{b}}^* \cdot \hat{\mathbf{b}}) \tag{8}$$

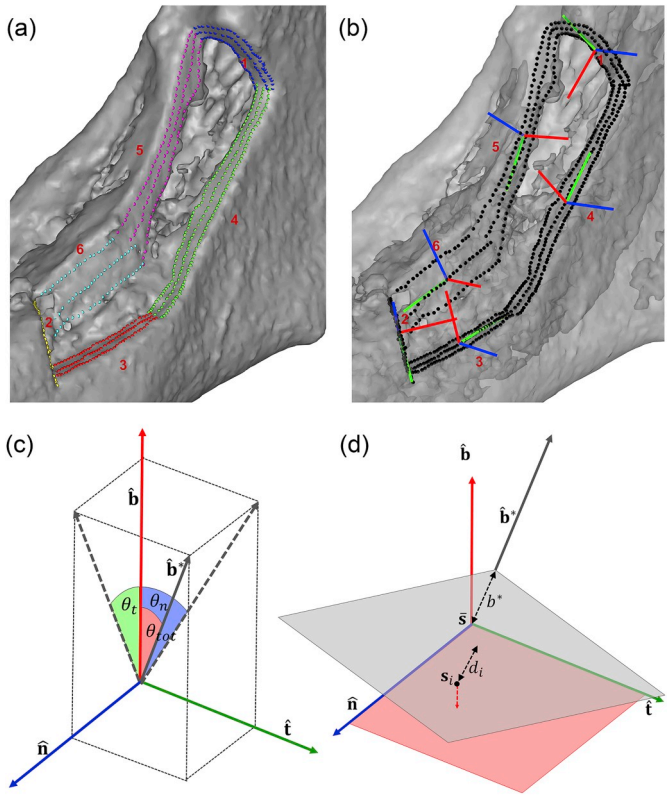

Fig. 3. Characterization of incision surfaces by manual sampling and definition of reference frames in the post-procedural mandibular model. (a) Sets of points sampled in different incisions are shown in different colors. The removed block is defined by one distal (1), one mesial (2), two apical (3, 4) and two cranial (5, 6) incisions. (b) Each set of points is associated with a reference frame identified by the principal axes of the point cloud, i.e., the effective binormal $\hat{\boldsymbol{b}}$ (red), the normal $\hat{\boldsymbol{n}}$ (blue), and the tangent $\hat{\boldsymbol{t}}$ (green). (c) Angle discrepancy components between the effective binormal and the planned binormal $\hat{\boldsymbol{b}}^*$ (grey vector). θ_{tot} (light red) is the total angle, θ_n (light blue) and θ_t (light green) are the angles between $\hat{\boldsymbol{b}}$ and the projections of $\hat{\boldsymbol{b}}^*$ (dashed grey vectors) on the planes orthogonal to $\hat{\boldsymbol{n}}$ and $\hat{\boldsymbol{t}}$, respectively. (d) The distance d_i of a sample point s_i from the planned plane (transparent grey), defined by $\hat{\boldsymbol{b}}^*$ and b^*, is indicated by the black dotted arrow. The red dotted line indicates the residual distance of s_i from the fitting plane (light red). (For interpretation of the references to color in this figure legend, the reader is referred to the Web version of this article.)

- *Inclination error around the normal axis*, which was measured as the angle between the effective binormal and the projection of the theoretical binormal on the plane orthogonal to $\hat{\mathbf{n}}$:

$$\theta_n = arccos\left(\frac{\hat{\mathbf{b}}^*\cdot\hat{\mathbf{b}}}{\sqrt{(\hat{\mathbf{b}}^*\cdot\hat{\mathbf{b}})^2+(\hat{\mathbf{b}}^*\cdot\hat{\mathbf{t}})^2}}\right) \tag{9}$$

- *Inclination error around the tangent axis*, which was measured as the *signed* angle between the effective binormal and the projection of the theoretical binormal on the plane orthogonal to $\hat{\mathbf{t}}$:

$$\theta_t = arcsin\left(\frac{\hat{\mathbf{b}}^*\cdot\hat{\mathbf{n}}}{\sqrt{(\hat{\mathbf{b}}^*\cdot\hat{\mathbf{b}})^2+(\hat{\mathbf{b}}^*\cdot\hat{\mathbf{n}})^2}}\right) \tag{10}$$

The angle θ_{tot} indicated the overall inclination error between the planned and effective planes. The angle θ_n specifically indicated the difference between the planned longitudinal direction (grossly the direction of scalpel movement from the start to the end of the incision) and the effective longitudinal direction of the incision. The angle θ_t indicated a discrepancy in the depth direction (direction of scalpel penetration), where a positive sign corresponded to a conservative incision, i.e. the inclination was such that less material was removed inside the bone. This inclination error was considered reliable only if the exposed surface had a certain depth (due to the thickness of the bone), or if the incision presented an in-plane curvature due to bone curvature.

The displacement errors informed about the shift between the effective and planned incision surfaces. As shown in Fig. 3(d), they were based on the signed distances $\{d_i\}$ of the N_s points $\{\mathbf{s}_i\}$ of each incision from the corresponding planned incision plane:

$$d_i = \mathbf{s}_i\cdot\hat{\mathbf{b}}^* - b^*. \tag{11}$$

Different statistics were obtained for each incision:

- The *mean distance error* averaged the signed distances:

$$\delta_{mean} = \frac{1}{N_s}\sum_{i=1}^{N_s} d_i \tag{12}$$

- The *root mean square distance error* was the root mean square (RMS) of the distances of the samples from the planned incision plane:

$$\delta_{RMS} = \sqrt{\frac{1}{N_s}\sum_{i=1}^{N_s} d_i^2} \tag{13}$$

- The *residual standard deviation* of the plane fitting to $\{\mathbf{s}_i\}$:

$$\sigma_b = \sqrt{\frac{1}{N_s}\sum_{i=1}^{N_s}((\mathbf{s}_i-\bar{\mathbf{s}})\cdot\hat{\mathbf{b}})^2} \tag{14}$$

The mean distance error (δ_{mean}) indicated the net displacement of the actual incision with respect to the planned incision. A positive mean corresponded to a conservative incision (less material removed). Conversely, the RMS error (δ_{RMS}) represented the whole deviation of the incision surface from the planned incision, being computed by the square of each distance. The residual standard deviation σ_b was the RMS of the sample distances from the effective incision plane, representing how well the incision surface lay on a single plane.

2.2.5. Confidence of the accuracy results

The validation procedure was subject to uncertainties arising from the segmentation, the registration, and the fitting of the effective cut planes.

The threshold based segmentation was affected by the finite native image resolution (0.3–0.4 mm) and by the presence of noise and artefacts on the image. The registration entailed an alignment error, even if gross artefacts were excluded by setting a cut-off threshold on the distance. The residual distances under the cut-off threshold represented the mismatch between the pre and post models, including not only the uncertainty of the registration parameters, but also of the segmentation procedure, since the intensity noise in pre and post CBCT/CT were uncorrelated. The RMS of the registration residuals were thus a good estimate of the error introduced in these phases of the validation.

The fitting of the effective plane to the samples was also associated to a finite confidence. Displacement error δ_{mean} was affected by the standard error of the plane position along the binormal direction, which was estimated as $\sigma_b/\sqrt{M}$, where $M \leq N_s$ represented the number of independent samples present in each incision. M was heuristically computed by dividing each sample sequence length by the native image resolution. Standard errors for angles θ_n, θ_t, and θ_{tot} were estimated from error propagation of the residual standard deviations σ_b, σ_t, and σ_n, where σ_t

and σ_n were computed similarly to Eq. (14) but substituting $\hat{\mathbf{t}}$ and $\hat{\mathbf{n}}$ to $\hat{\mathbf{b}}$, respectively.

3. Results

3.1. Segmentation

The segmented models of the mandible from pre and post-procedural images are shown in Fig. 4, including the cadaver skull (first row) and the two patients (second and third rows). Differences between the pre ($\mathcal{M}_{pre}$) and post ($\mathcal{M}_{post}$) models were present in the harvesting site and in smaller details, as a consequence of the star artefacts produced by dental restoration materials or of alterations caused by dental interventions occurred between data acquisitions. The osteotomy surfaces resulted better delineated in the soft bone post-procedural model $\mathcal{M}_{soft}$ than in $\mathcal{M}_{post}$, since the lower segmentation threshold included more cancellous bone, albeit avoiding CBCT/CT signal artefacts.

3.2. Registration

The registration performance is shown in Fig. 5, where the contour plots of the registered cortical mandible models and surgical guide are superimposed to the native post-procedural tomographic images in axial and coronal slices. A mismatch between pre ($\mathcal{M}_{pre}$) and post ($\mathcal{M}_{post}$) models is noticeable only in a minority of regions, where the dental treatments (including bone removal) or acquisition artefacts caused an alteration of the model geometry, whereas the majority of the surface aligned with submillimeter accuracy. The distance cutoff threshold of 2 mm, used in the refinement phase, permitted the exclusion from the registration of the part of the model altered from pre to post-procedural condition. Quality control on the registration results was provided by the statistics on the residual distance values, reported in Table 1 for the four cases. A high portion (97–99%) of the model surface showed proper geometrical match, i.e. residual distance $\leq$2 mm. In this region, the residual inter-model distance was distributed according to a RMS of 0.3–0.4 mm, a median of 0.1–0.2 mm, and a 90 percentile under 0.6 mm. The achieved accuracy was consistent with the original CBCT/CT data

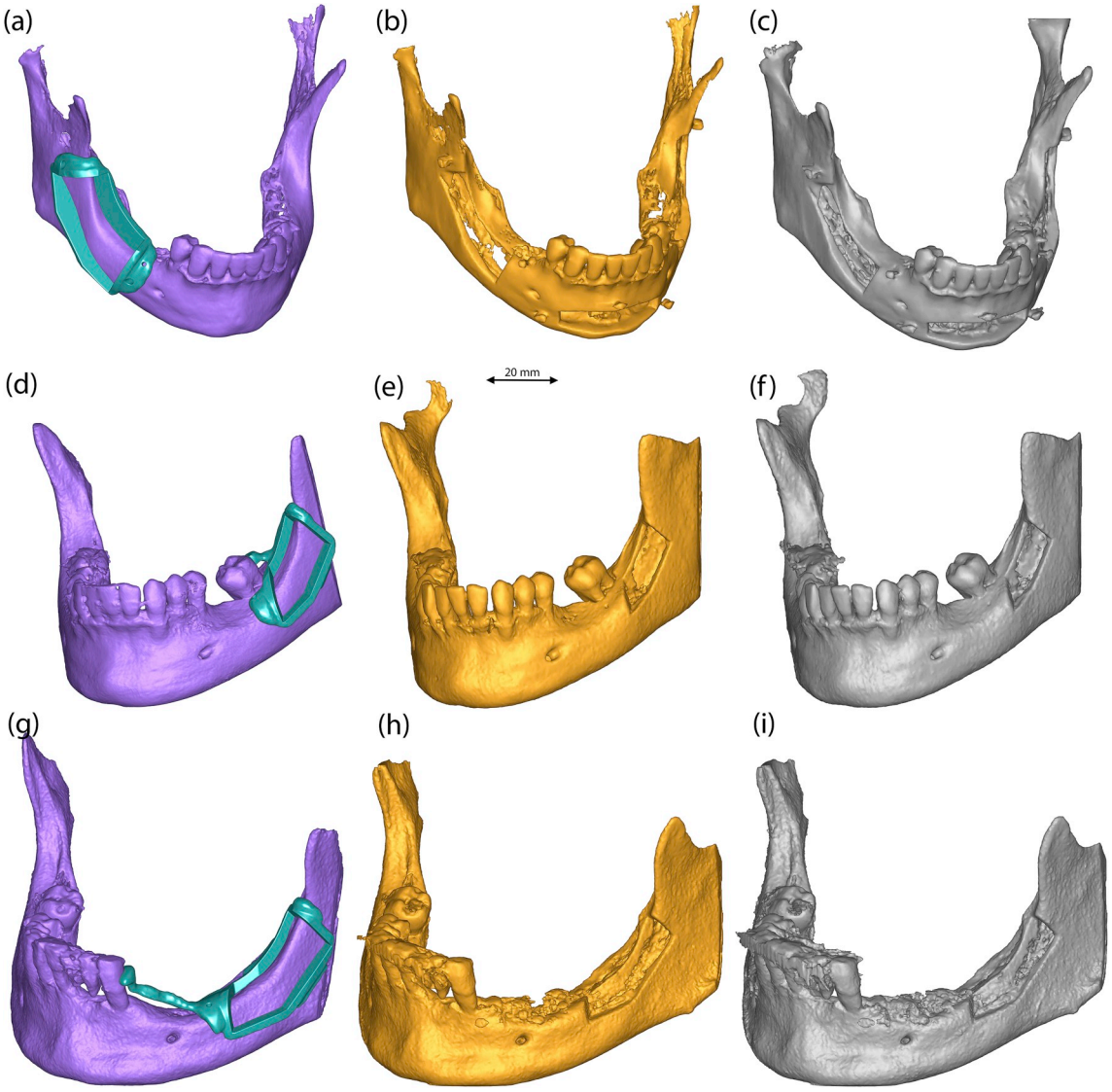

Fig. 4. Segmentation of the mandible of the cadaveric skull (a, b, and c), evidencing the incision of case 1, and of patient cases 3 (d, e, and f), and 4 (g, h, and i). In the first column, the pre-procedural cortical bone models $\mathcal{M}_{pre}$ and corresponding virtual guides are shown in purple and cyan, respectively. The post-procedural cortical $\mathcal{M}_{post}$ (second column) and soft $\mathcal{M}_{soft}$ (third column) bone models are shown in orange and grey, respectively. The harvesting sites are observable in the ramus region of the post models, in correspondence of the surgical procedure. (For interpretation of the references to color in this figure legend, the reader is referred to the Web version of this article.)

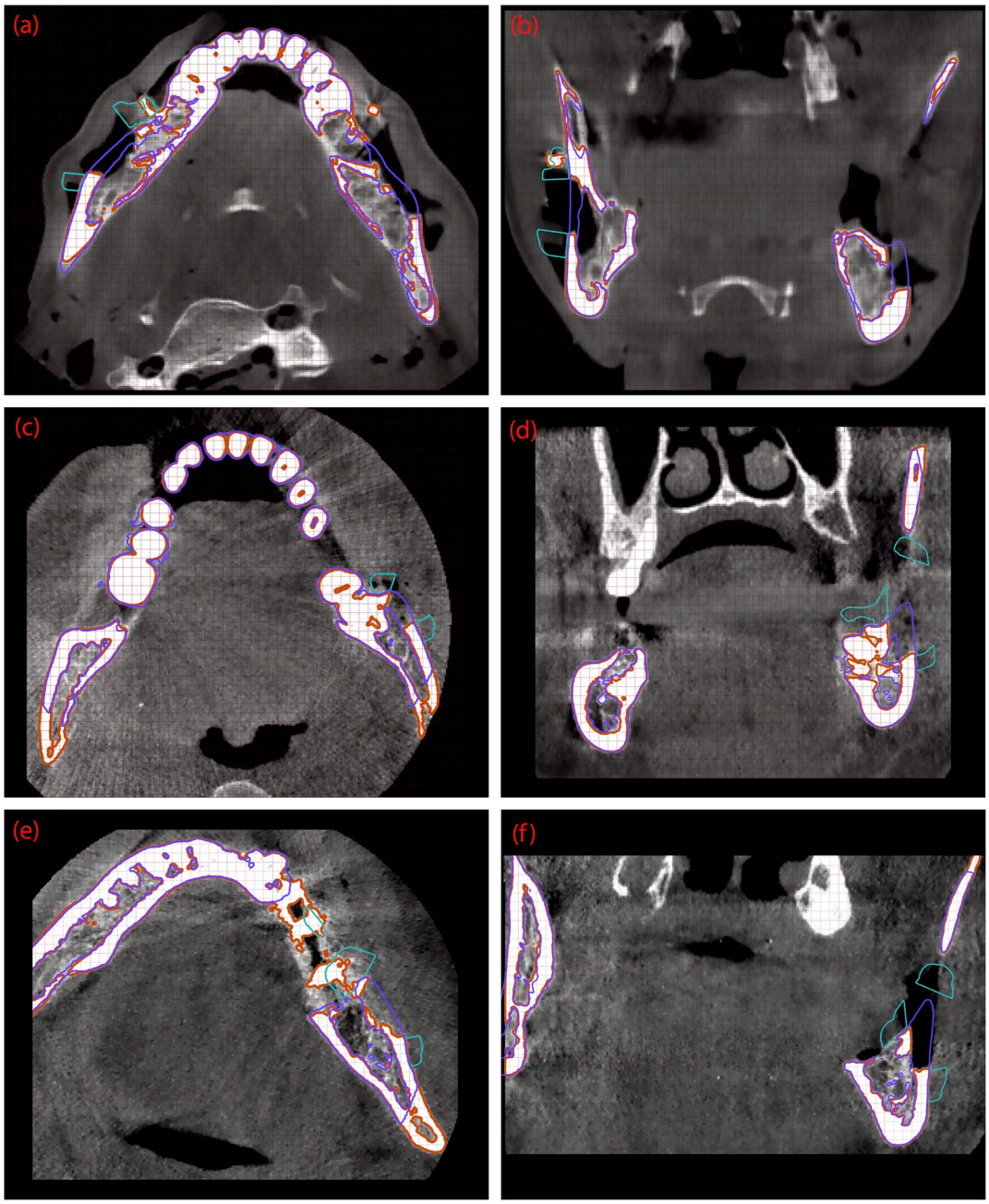

Fig. 5. Results of the registration of the mandibular models for the cadaveric case 1 (a, b), and the patient cases 3 (c, d), and 4 (e, f), shown as contour lines superimposed to post-procedural axial (a, c, e) and coronal (b, d, f) CBCT/CT slices, windowed between −400 and 1200 grayscale values. The pre-procedural model $\mathscr{M}_{pre}$ and the corresponding virtual guide are drawn in purple and cyan, respectively, while the post-procedural model $\mathscr{M}_{post}$ is indicated in orange. The grid step is 2 mm. (For interpretation of the references to color in this figure legend, the reader is referred to the Web version of this article.)

Table 1
Case list with segmentation parameters and quality parameters resulting from registration of pre and post-procedural mandibular models.

Case number	Mandibular side	CT Resolution (mm)	Hard and soft segmentation thresholds	Registration results: residual distance statistics			
				Fraction under 2 mm cutoff (%)	RMS (mm)	Median (mm)	90 percentile (mm)
1	right	0.4	1000–600	97	0.393	0.182	0.502
2	left	0.4	1000–600	97	0.415	0.189	0.558
3	left	0.3	1200–800	99	0.402	0.179	0.593
4	left	0.3	1000–700	98	0.306	0.124	0.361

RMS = root mean square.

resolution (0.3–0.4 mm). Of note, the RMS distance between registered $\mathcal{M}_{pre}$ models in cases 1 and 2, which shared the same cadaver skull but had the segmentation and registration operations performed separately, was <0.01 mm, indicating a good reproducibility of the procedure.

3.3. Incision accuracy estimation

A visual assessment of the harvesting accuracy can be appreciated in Fig. 6, where the registered virtual guide (cyan) is superimposed to the soft bone mandibular model. The incision surfaces are evidenced by the sample points. Three of the harvesting sites were on the left side of the mandible and one on the right side. Each block was composed of a variable number of incisions (4–6), with the additional incisions on the apical or cranial position. For the two patient cases (panels c and d), tooth anchoring of the surgical guide was employed. Some irregularity of the exposed surfaces was observable, especially on the corners between adjacent incisions. The quantitative validation was performed on each incision by measuring angular and displacement discrepancies between the sample points and the planned incisions of the virtual guide, as shown for two representative planes in Fig. 7. Mesial and distal incisions were characterized by a more isotropic spread of the samples on the incision plane, due to the more consistent thickness and curvature of the exposed bone (panel a). Differently, most cranial and apical incisions tended to be linear, with a minor spread of the sample points along the normal direction (panel b). Accuracy results for the whole datasets are reported in Table 2. The total (θ_{tot}), around-normal (θ_n), and around-tangent (θ_t) angular errors averaged 8.1 ± 6.7, 3.4 ± 5.6, and -1.8 ± 8.5 deg, respectively. The around-tangent inclination generally dominated the angular errors in cranial and apical incisions, due to the minor sample spread along the normal axis. The mean (δ_{mean}) and RMS (δ_{RMS}) distance errors averaged 0.20 ± 0.76 and 0.76 ± 0.48 mm, respectively, while the residual standard deviation σ_b of the incision plane averaged 0.25 ± 0.24 mm. For the displacement error δ_{mean}, the confidence intervals were very narrow (<0.1 mm), and below data resolution and registration error (0.4 mm), suggesting that the presented validation methodology was suitable for estimating the accuracy of the guided harvesting procedure. Angular confidence intervals were inferior to 2 deg for the majority of examined incisions, with the exception of the few cases where the bone surface was very irregular (e.g., case 1 distal) or very thin and linear (e.g., case 2 apical II), compromising the determination of the depth inclination.

4. Discussion

4.1. Mandibular guided bone harvesting

The major limitation of conventional freehand mandibular osteotomy is the safety margin required in order to avoid damage to anatomical structures, reducing the potential volume of harvestable bone. Conservative cut patterns with limited depth have been suggested to avoid interference with the alveolar nerve and other underlying structures [9,13], promoting a fracture of the bone block instead. This practice however entails further risks and intraoperative patient discomfort. The introduction of the 3D computer planning of the whole osteotomy geometry allows for a more extensive use of the cutting tools, which are safely guided by the lithographic template away from delicate structures [24]. Indeed, the osteotomy can be customized to the specific patient, permitting the maximization of the block dimensions while preserving safety margins, and consistently reducing the fracture approach.

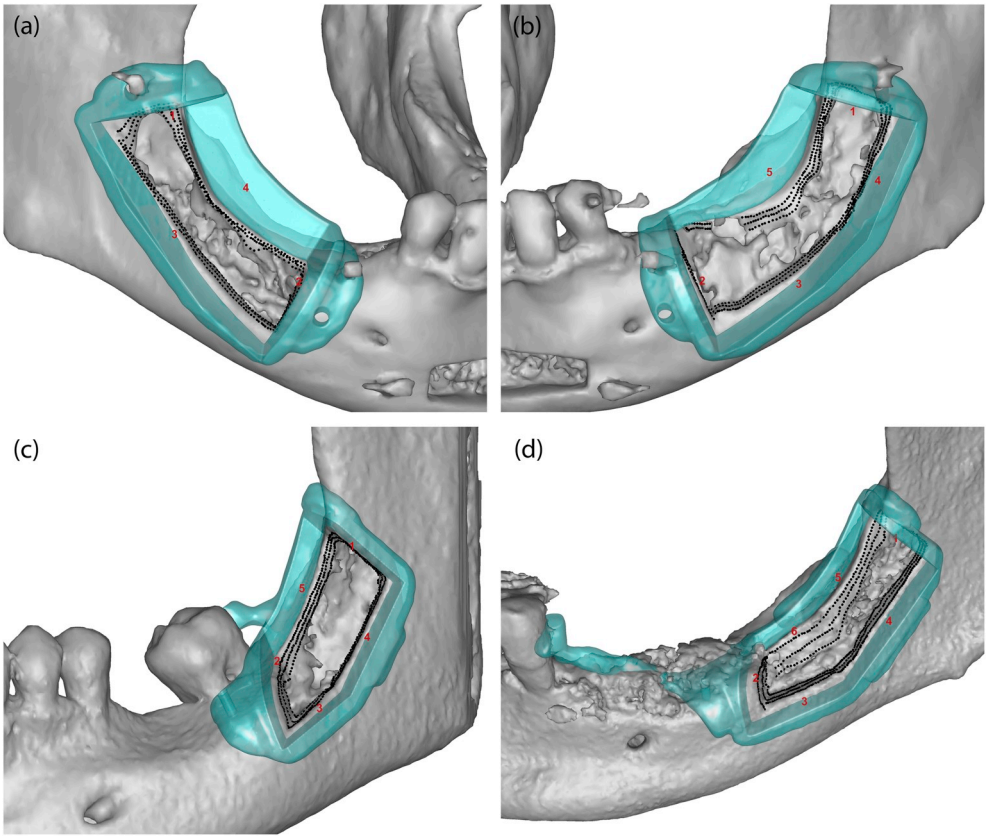

Fig. 6. Accuracy assessment of bone block harvesting by comparison of the registered virtual guide (semitransparent cyan) and the post-procedural soft bone model (solid grey), in the cadaveric skull cases 1 (a) and 2 (b), and in the patient cases 3 (c) and 4 (d). Each incision surface is numbered in red and identified by the corresponding sample points (black). (For interpretation of the references to color in this figure legend, the reader is referred to the Web version of this article.)

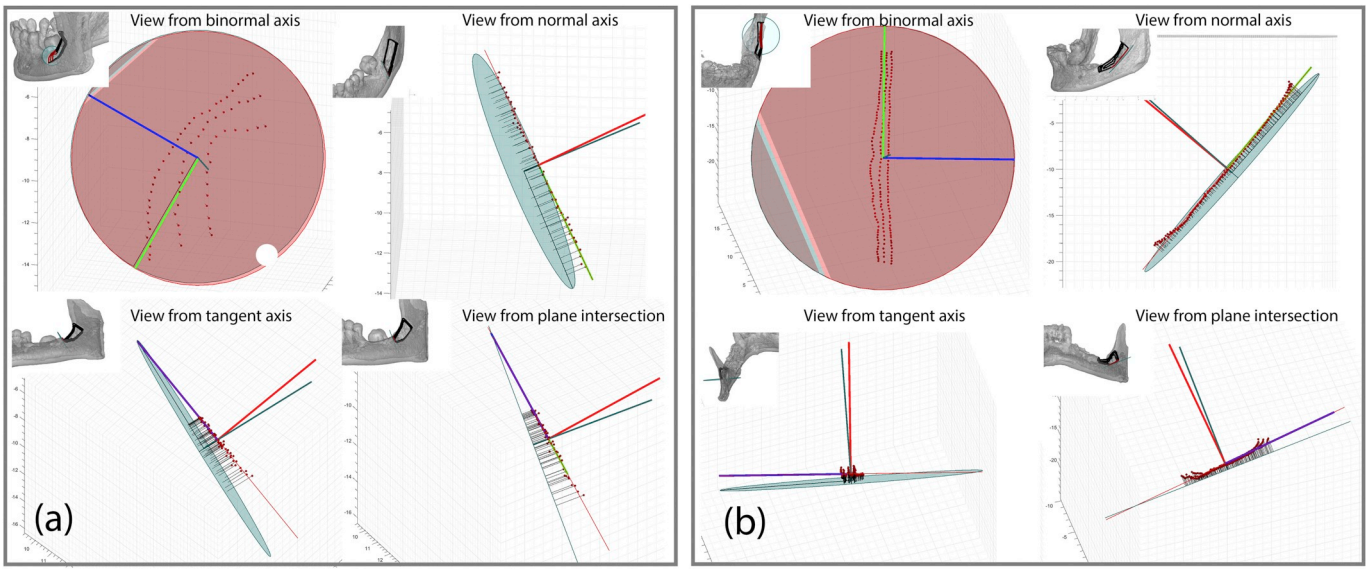

Fig. 7. Representative examples of incision accuracy estimation by comparison of planned (cyan) and effective (red) incision planes. Corresponding binormal axes are shown in the same colors, while the normal and tangent axes are in blue and green, respectively. Incision samples are represented as red dots, and their distance from the theoretical plane as black segments. The view from the binormal axis reveals overall sample spread, the views from the normal and tangent axes highlight the normal and tangent angular errors, and the view from the plane intersection evidences the sample displacements and the total angular error. (a) Case 3, mesial incision. (b) Case 4, apical II incision. (For interpretation of the references to color in this figure legend, the reader is referred to the Web version of this article.)

Table 2
Results of guided bone harvesting accuracy for each incision. Angular and displacement errors (bold) are reported together with the corresponding confidence.

Case number	Incision	Angular errors (deg)			Distance errors (mm)		Residual STD σ_b (mm)
		θ_{tot}	θ_n	θ_t	δ_{mean}	δ_{RMS}	
1	1 Dist	**33.2** ± 4.6	**26.4** ± 2.9	**−23.1** ± 3.5	**1.01** ± 0.15	**1.72**	**1.02**
	2 Mesi	**7.3** ± 0.6	**1.3** ± 0.2	**−7.2** ± 0.6	**−0.61** ± 0.01	**0.62**	**0.07**
	3 Apic	**5.0** ± 1.0	**2.3** ± 0.1	**4.5** ± 1.0	**0.43** ± 0.01	**0.61**	**0.18**
	4 Cran	**1.2** ± 0.5	**0.5** ± 0.1	**−1.1** ± 0.5	**−0.07** ± 0.01	**0.17**	**0.14**
2	1 Dist	**16.3** ± 3.3	**6.5** ± 0.7	**15.1** ± 3.2	**−1.62** ± 0.05	**1.69**	**0.33**
	2 Mesi	**11.6** ± 0.9	**2.8** ± 0.2	**−11.3** ± 0.9	**0.01** ± 0.02	**0.31**	**0.16**
	3 Apic I	**5.9** ± 2.3	**5.5** ± 0.3	**2.0** ± 2.3	**0.69** ± 0.04	**0.94**	**0.37**
	4 Apic II	**11.1** ± 4.4	**0.9** ± 0.5	**11.0** ± 4.4	**0.32** ± 0.07	**0.67**	**0.76**
	5 Cran	**4.6** ± 0.6	**2.9** ± 0.2	**3.5** ± 0.6	**0.19** ± 0.03	**0.60**	**0.41**
3	1 Dist	**1.1** ± 0.9	**0.7** ± 0.3	**−0.9** ± 0.9	**−0.13** ± 0.02	**0.18**	**0.15**
	2 Mesi	**7.9** ± 0.6	**2.5** ± 0.2	**7.5** ± 0.6	**0.72** ± 0.01	**0.74**	**0.08**
	3 Apic I	**8.1** ± 1.4	**3.5** ± 0.4	**−7.3** ± 1.4	**0.56** ± 0.02	**0.60**	**0.13**
	4 Apic II	**7.4** ± 1.4	**0.2** ± 0.2	**−7.4** ± 1.4	**0.35** ± 0.02	**0.38**	**0.17**
	5 Cran	**9.7** ± 0.8	**0.5** ± 0.1	**−9.7** ± 0.8	**0.04** ± 0.01	**0.12**	**0.09**
4	1 Dist	**3.5** ± 0.8	**0.9** ± 0.4	**3.3** ± 0.7	**−1.62** ± 0.02	**1.63**	**0.16**
	2 Mesi	**6.0** ± 0.6	**1.9** ± 0.3	**5.7** ± 0.5	**1.34** ± 0.01	**1.35**	**0.09**
	3 Apic I	**6.4** ± 0.9	**1.8** ± 0.2	**−6.1** ± 0.9	**1.05** ± 0.01	**1.06**	**0.11**
	4 Apic II	**3.8** ± 1.5	**1.5** ± 0.1	**−3.5** ± 1.5	**0.71** ± 0.02	**0.77**	**0.24**
	5 Cran I	**4.3** ± 0.5	**0.2** ± 0.1	**−4.3** ± 0.5	**0.66** ± 0.01	**0.66**	**0.08**
	6 Cran II	**8.3** ± 0.9	**5.5** ± 0.4	**−6.2** ± 0.8	**−0.06** ± 0.02	**0.37**	**0.17**
Mean ± STD		**8.1 ± 6.7**	**3.4 ± 5.6**	**−1.8 ± 8.5**	**0.20 ± 0.76**	**0.76 ± 0.48**	**0.25 ± 0.24**

Dist = distal, Mesi = mesial, Apic = apical, Cran = cranial, STD = standard deviation.

The validation framework proposed in this study aimed at being an instrument to assess the accuracy of the bone harvesting procedure, and in its preliminary testing proved a suitable detector of the discrepancy between planned and performed surgical intervention. The methodology relied on the registration of pre-procedural and post-procedural bone models obtained from CBCT/CT images. Intra-procedural registration techniques have been proposed in order to increase the accuracy of computer guided systems [39,40]. In our case the alignment was a prerequisite for the post-procedural assessment, and required high accuracy to avoid adding spurious errors to those inherent to the osteotomy alone. Although intensity based registration approaches are generally considered more robust than those involving only a subset of features, especially in multimodal imaging [41], we preferred a surface based registration that allowed the alignment of the specific rigid structure of interest, avoiding the interference of nearby soft tissue and the other movable skull parts. However, since the incision accuracy measurement is independent from the registration approach, other methods, e.g. voxel-based, could be favored, according to preference and software availability. The stochastic multi-trial implementation of the ICP algorithm granted efficacy in avoiding local minima of the target function, increasing the registration precision and robustness. The cutoff threshold prevented the intra-procedural bone alterations, which are expected not to match, to influence the fine alignment of the matching anatomy.

Traditional validation approaches of computer-assisted implant surgery are based on the definition of a reference system, dependent on

the location of the implant, which defines metric and angular deviations significant to the specific context of implant placement [16–18]. Similarly, the presented set of discrepancy metrics covers different aspects of clinical significance, being tailored to the problematics of osteotomy. While the RMS displacement error (δ_{RMS}) represents a general deviation from the optimal incision surface, the signed average displacement (δ_{mean}) discriminates between a conservative resection, having no adverse effects apart from the minor graft volume, and an excessive bone removal, which may have critical consequences on the intervention outcome. The residual standard deviation (σ_b) may be considered a quality parameter for plane fitting of the incision surface, thus constituting a detector of deviations from cut flatness and a measure of scalpel movement irregularity. The angular deviation is also separated into components, which bear specific clinical implications. The signed around-tangent angular error (θ_t) is indicative of conservative or excessive removal of cancellous bone deep into the block, since it is measured on the cortical side of the bone. Conversely, the around-normal angular error (θ_n) characterizes the obliquity of incisions, indicating a difference in resected material from one cut end to the other, complementing the safety implications given by the average displacement error. Both signed discrepancies δ_{mean} and θ_t are particularly important for the apical cut, where excessive bone harvesting may cause consistent risk of nerve damage. Of note, all the possible mismatch contributions described above (shift, inclination, and non-planarity of the cut), affect the RMS error (δ_{RMS}), which may be considered the detector of overall discrepancy.

Regarding the reliability of the discrepancy values, the confidence interval for the detection of the incision geometry via plane interpolation resulted inferior to the image resolution of the data used for both planning and validation (0.3 mm for the tested cases). Since such submillimetric accuracy may be considered sufficient for adequately planning and assessing dental implant surgical procedures [16,17,20,42], we can conclude that the proposed framework is a promising tool for quantifying the accuracy of guided bone harvesting techniques. Once applied to a large number of cases, accuracy statistics may contribute to the assessment of the safety margins within which the surgical planning can be performed.

4.2. General guided surgery applications

The accuracy assessment framework presented in this study could be adapted to other scenarios than mandibular bone harvesting. In the field of dental medicine, the use of 3D printed cutting guides has been also reported for sinus grafting [43,44] and mesiodens extraction [45]. More in general, patient-specific osteotomy guides have been considered as an aid for bone osteotomy in different bone surgical setting [46–48]. They have the potential of fully translating the treatment plan to the execution phase, obtaining outcomes that are more predictable than the freehand procedure and less dependent on the surgeon experience, and the capability of reducing operating room times as well. Cranial and maxillofacial surgery can avail of these techniques [49–52], particularly for mandibular reconstruction, e.g. Refs. [53–55]. Examples in orthopedic treatments include femoral neck [56,57], distal femoral [58,59], and high tibial [60,61] osteotomy, corrective limb surgery [62,63], and knee arthroplasty [64,65]. Bone tumor resection may also benefit from printed custom guides [66–70]. However, as the literature suggests, the final clinical outcome strongly depends on the accuracy of the guide and its placement [46], which can vary considerably according to the system utilized and the time between the planning scan and the surgery execution. A framework to exhaustively quantify guide accuracy is therefore necessary to fully understand the effective convenience of these techniques in the clinical setting. The proposed framework could be applied to assess the accuracy of these procedures, provided that the design of the guide on pre-procedural CT data is constituted of planar cutting surfaces, and a post-procedural CT is available. On the other hand, the direction of the normal and tangent reference axes would be defined according to the requirements of the specific anatomical context. More in general, the presented validation procedure may be suitable to evaluate the accuracy of any flat resection interventions aided by virtual planning and 3D-navigation, even without the mediation of any printed physical guide, since only the pre-procedural anatomy/virtual plan and the post-procedural anatomy are in fact required as input data.

4.3. Study limitations

The accuracy framework was tested on a limited number of cases. However, the aim of the present study was to evidence the feasibility and applicability of the framework in a practical scenario, not to provide a complete assessment of a specific bone collection technique. Even if the number of cases was limited, it should be considered that 4 to 6 cut planes were assessed for accuracy in each case, for a total of 20 planes.

The native image quality provided by CBCT scan was the major limitation to further improve the confidence interval of the assessment framework. It is however expected that any guided technique cannot outperform its native data resolution, making a finer discrepancy detection redundant. The inaccuracy of current CBCT systems in providing absolute bone density as grey levels may constitute an additional source of operator-dependent segmentation error, as the thresholds need to be readjusted if a different system is used. This problem is intrinsic in bone evaluation during surgical planning with CBCT. Acquiring the pre and post images on the same machine can facilitate the segmentation of corresponding anatomies.

Registration quality was quantified in terms of the residual similarity measures utilized by the registration itself, which may underestimate any real target registration error based on independent landmarks. It is to note, however, that the definition of specific landmarks would be time consuming and would involve additional segmentation errors. Furthermore, the residual RMS distance was analyzed in relation to the fraction under the 2 mm cutoff, which, acting as a proximity detector between surfaces of complex shape, would easily identify major misalignments missed by visual inspection.

On the other hand, our procedure is able to produce a statistically sound accuracy assessment of a CAD-planned osteotomy on a large cohort of cases, requiring only follow-up tomographic imaging as additional data, which may be a major advantage. This is considerably less invasive and more feasible than other approaches typical of in situ surgical validations.

4.4. Conclusions

A quantitative framework to estimate the accuracy of bone block harvesting guided by a computer-planned lithographic template was presented and tested. The framework allowed the determination of the osteotomy accuracy by the quantitative measure of angular and displacement errors between the planned and real bone incisions. A set of quality parameters for the accuracy assessment was also identified, in terms of registration errors and confidence of fitting, in order to establish the reliability of the results.

The proposed framework was validated on four cases, demonstrating its capability to quantify the tolerance associated with computer-guided bone harvesting techniques. Its application to a larger cohort of cases may allow to identify safety margins for surgical guide planning and to perform an accuracy comparison between different bone harvesting techniques.

Acknowledgments

The study has been developed under the Healthcare Research and Innovation Program (IRCS-FBK-PAT), funded by the Autonomous Province of Trento, Italy.

The study uses anonymized patient CT images collected during

standard procedures of diagnosis and follow up. Informed consent was given for the use of the images, in agreement with the local statutory requirements.

References

[1] M.S. Tonetti, C.H.F. Hämmerle, C. European Workshop on Periodontology Group, Advances in bone augmentation to enable dental implant placement: consensus report of the sixth european workshop on periodontology, J. Clin. Periodontol. 35 (2008) 168–172, https://doi.org/10.1111/j.1600-051X.2008.01268.x.

[2] A.T. Jensen, S.S. Jensen, N. Worsaae, Complications related to bone augmentation procedures of localized defects in the alveolar ridge. A retrospective clinical study, Oral Maxillofac. Surg. 20 (2016) 115–122, https://doi.org/10.1007/s10006-016-0551-8.

[3] M. Chiapasco, M. Zaniboni, L. Rimondini, Autogenous onlay bone grafts vs. alveolar distraction osteogenesis for the correction of vertically deficient edentulous ridges: a 2-4-year prospective study on humans, Clin. Oral Implant. Res. 18 (2007) 432–440, https://doi.org/10.1111/j.1600-0501.2007.01351.x.

[4] S.S. Jensen, H. Terheyden, Bone augmentation procedures in localized defects in the alveolar ridge: clinical results with different bone grafts and bone-substitute materials, Int. J. Oral Maxillofac. Implant. 24 (Suppl) (2009) 218–236.

[5] R. Pistilli, P. Felice, M. Piatelli, A. Nisii, C. Barausse, M. Esposito, Blocks of autogenous bone versus xenografts for the rehabilitation of atrophic jaws with dental implants: preliminary data from a pilot randomised controlled trial, Eur. J. Oral Implant. 7 (2014) 153–171.

[6] A. Sakkas, F. Wilde, M. Heufelder, K. Winter, A. Schramm, Autogenous bone grafts in oral implantology—is it still a "gold standard"? A consecutive review of 279 patients with 456 clinical procedures, Int J Implant Dent 3 (2017), https://doi.org/10.1186/s40729-017-0084-4.

[7] N. Altiparmak, S.S. Soydan, S. Uckan, The effect of conventional surgery and piezoelectric surgery bone harvesting techniques on the donor site morbidity of the mandibular ramus and symphysis, Int. J. Oral Maxillofac. Surg. 44 (2015) 1131–1137, https://doi.org/10.1016/j.ijom.2015.04.009.

[8] A. Sakkas, K. Ioannis, K. Winter, A. Schramm, F. Wilde, Clinical results of autologous bone augmentation harvested from the mandibular ramus prior to implant placement. An analysis of 104 cases, GMS Interdiscip Plast Reconstr Surg DGPW 5 (2016), https://doi.org/10.3205/iprs000100.

[9] J. Clavero, S. Lundgren, Ramus or chin grafts for maxillary sinus inlay and local onlay augmentation: comparison of donor site morbidity and complications, Clin. Implant Dent. Relat. Res. 5 (2003) 154–160.

[10] E. Nkenke, F.W. Neukam, Autogenous bone harvesting and grafting in advanced jaw resorption: morbidity, resorption and implant survival, Eur. J. Oral Implant. 7 (Suppl 2) (2014) S203–S217.

[11] D. Reininger, C. Cobo-Vázquez, M. Monteserín-Matesanz, J. López-Quiles, Complications in the use of the mandibular body, ramus and symphysis as donor sites in bone graft surgery. A systematic review, Med. Oral, Patol. Oral Cirugía Bucal 21 (2016) e241–249.

[12] R. Jacobs, B. Salmon, M. Codari, B. Hassan, M.M. Bornstein, Cone beam computed tomography in implant dentistry: recommendations for clinical use, BMC Oral Health 18 (2018) 88, https://doi.org/10.1186/s12903-018-0523-5.

[13] L. Cordaro, F. Torsello, M.T. Miuccio, V.M. di Torresanto, D. Eliopoulos, Mandibular bone harvesting for alveolar reconstruction and implant placement: subjective and objective cross-sectional evaluation of donor and recipient site up to 4 years, Clin. Oral Implant. Res. 22 (2011) 1320–1326, https://doi.org/10.1111/j.1600-0501.2010.02115.x.

[14] A. Tahmaseb, D. Wismeijer, W. Coucke, W. Derksen, Computer technology applications in surgical implant dentistry: a systematic review, Int. J. Oral Maxillofac. Implant. 29 (Suppl) (2014) 25–42, https://doi.org/10.11607/jomi.2014suppl.g1.2.

[15] J. D'haese, J. Ackhurst, D. Wismeijer, H. De Bruyn, A. Tahmaseb, Current state of the art of computer-guided implant surgery, Periodontol 73 (2000) 121–133, https://doi.org/10.1111/prd.12175, 2017.

[16] D. Schneider, P. Marquardt, M. Zwahlen, R.E. Jung, A systematic review on the accuracy and the clinical outcome of computer-guided template-based implant dentistry, Clin. Oral Implant. Res. 20 (Suppl 4) (2009) 73–86, https://doi.org/10.1111/j.1600-0501.2009.01788.x.

[17] J. D'haese, T.V.D. Velde, A. Komiyama, M. Hultin, H.D. Bruyn, Accuracy and complications using computer-designed stereolithographic surgical guides for oral rehabilitation by means of dental Implants: a review of the literature, Clin. Implant Dent. Relat. Res. 14 (2012) 321–335, https://doi.org/10.1111/j.1708-8208.2010.00275.x.

[18] N. Van Assche, M. Vercruyssen, W. Coucke, W. Teughels, R. Jacobs, M. Quirynen, Accuracy of computer-aided implant placement, Clin. Oral Implant. Res. 23 (Suppl 6) (2012) 112–123, https://doi.org/10.1111/j.1600-0501.2012.02552.x.

[19] F. Bover-Ramos, J. Viña-Almunia, J. Cervera-Ballester, M. Peñarrocha-Diago, B. García-Mira, Accuracy of implant placement with computer-guided surgery: a systematic review and meta-analysis comparing cadaver, clinical, and in vitro studies, Int. J. Oral Maxillofac. Implant. 33 (2018) 101–115, https://doi.org/10.11607/jomi.5556.

[20] D.A.A. Marlière, M.S. Demétrio, L.S. Picinini, R.G. De Oliveira, H.D.D.M. Chaves Netto, Accuracy of computer-guided surgery for dental implant placement in fully edentulous patients: a systematic review, Eur. J. Dermatol. 12 (2018) 153–160, https://doi.org/10.4103/ejd.ejd_249_17.

[21] C. Seo, G. Juodzbalys, Accuracy of guided surgery via stereolithographic mucosa-supported surgical guide in implant surgery for edentulous patient: a systematic review, J. Oral Maxillofac. Res. 9 (2018), https://doi.org/10.5037/jomr.2018.9101.

[22] L. De Stavola, A. Fincato, inventors; Method for making a surgical guide for bone harvesting, International Patent WO (2014 Nov 27) 1–55. International Publication No.: WO/2014/188369 A1, International Application No.: PCT/IB2014/061624.

[23] L. De Stavola, A. Fincato, A.M. Albiero, A computer-guided bone block harvesting procedure: a proof-of-principle case report and technical notes, Int. J. Oral Maxillofac. Implant. 30 (2015) 1409–1413, https://doi.org/10.11607/jomi.4045.

[24] L. De Stavola, A. Fincato, E. Bressan, L. Gobbato, Results of computer-guided bone block harvesting from the mandible: a case series, Int. J. Periodontics Restor. Dent. 37 (2017) e111–e119, https://doi.org/10.11607/prd.2721.

[25] L. De Stavola, J. Tunkel, Results of vertical bone augmentation with autogenous bone block grafts and the tunnel technique: a clinical prospective study of 10 consecutively treated patients, Int. J. Periodontics Restor. Dent. 33 (2013) 651–659, https://doi.org/10.11607/prd.0932.

[26] R.C. Gonzalez, R.E. Woods, Digital Image Processing, third ed., Prentice-Hall, Inc., Upper Saddle River, NJ, USA, 2006.

[27] L.G. Shapiro, Connected component labeling and adjacency graph construction, in: T.Y. Kong, A. Rosenfeld (Eds.), Mach. Intell. Pattern Recognit., vol. 19, North-Holland, 1996, pp. 1–30, https://doi.org/10.1016/S0923-0459(96)80011-5.

[28] J.V. Hajnal, D.L.G. Hill, Medical Image Registration, CRC Press, 2001.

[29] H. Jiang, R.A. Robb, K.S. Holton Tainter, New Approach to 3-D Registration of Multimodality Medical Images by Surface Matching, vol. 1808, 1992, pp. 196–213, https://doi.org/10.1117/12.131078.

[30] A. Cristoforetti, M. Masè, L. Faes, M. Centonze, M.D. Greco, Renzo Antolini, et al., A stochastic approach for automatic registration and fusion of left atrial electroanatomic maps with 3D CT anatomical images, Phys. Med. Biol. 52 (2007) 6323, https://doi.org/10.1088/0031-9155/52/20/015.

[31] F. Ravelli, M. Masè, A. Cristoforetti, M. Del Greco, M. Centonze, M. Marini, et al., Anatomic localization of rapid repetitive sources in persistent atrial fibrillation: fusion of biatrial CT images with wave similarity/cycle length maps, JACC Cardiovasc Imaging 5 (2012) 1211–1220, https://doi.org/10.1016/j.jcmg.2012.07.016.

[32] Y. Chen, G. Medioni, Object modeling by registration of multiple range images, IEEE Int. Conf. Robot. Autom. Proc. 3 (1991) 2724–2729, https://doi.org/10.1109/ROBOT.1991.132043, 1991.

[33] P.J. Besl, N.D. McKay, A method for registration of 3-D shapes, IEEE Trans. Pattern Anal. Mach. Intell. 14 (1992) 239–256, https://doi.org/10.1109/34.121791.

[34] J.M. Fitzpatrick, J.B. West, C.R. Maurer, Predicting error in rigid-body point-based registration, IEEE Trans. Med. Imaging 17 (1998) 694–702, https://doi.org/10.1109/42.736021.

[35] P.H. Schönemann, A generalized solution of the orthogonal procrustes problem, Psychometrika 31 (1966) 1–10, https://doi.org/10.1007/BF02289451.

[36] S. Umeyama, Least-squares estimation of transformation parameters between two point patterns, IEEE Trans. Pattern Anal. Mach. Intell. 13 (1991) 376–380, https://doi.org/10.1109/34.88573.

[37] D.W. Eggert, A. Lorusso, R.B. Fisher, Estimating 3-D rigid body transformations: a comparison of four major algorithms, Mach. Vis. Appl. 9 (1997) 272–290, https://doi.org/10.1007/s001380050048.

[38] C.T. Huang, O.R. Mitchell, A Euclidean distance transform using grayscale morphology decomposition, IEEE Trans. Pattern Anal. Mach. Intell. 16 (1994) 443–448, https://doi.org/10.1109/34.277600.

[39] W. Birkfellner, P. Solar, A. Gahleitner, K. Huber, F. Kainberger, J. Kettenbach, et al., In-vitro assessment of a registration protocol for image guided implant dentistry, Clin. Oral Implant. Res. 12 (2001) 69–78.

[40] T. Flügge, W. Derksen, J. Te Poel, B. Hassan, K. Nelson, D. Wismeijer, Registration of cone beam computed tomography data and intraoral surface scans - a prerequisite for guided implant surgery with CAD/CAM drilling guides, Clin. Oral Implant. Res. 28 (2017) 1113–1118, https://doi.org/10.1111/clr.12925.

[41] W. Birkfellner, M. Figl, H. Furtado, A. Renner, S. Hatamikia, J. Hummel, Multi-modality imaging: a software fusion and image-guided therapy perspective, Front. Physiol. 6 (2018), https://doi.org/10.3389/fphy.2018.00066.

[42] E. Naziri, A. Schramm, F. Wilde, Accuracy of computer-assisted implant placement with insertion templates, GMS Interdiscip Plast Reconstr Surg DGPW 5 (2016) Doc15, https://doi.org/10.3205/iprs000094.

[43] G.A. Mandelaris, A.L. Rosenfeld, Alternative applications of guided surgery: precise outlining of the lateral window in antral sinus bone grafting, J Oral Maxillofac Surg Off J Am Assoc Oral Maxillofac Surg 67 (2009) 23–30, https://doi.org/10.1016/j.joms.2009.07.006.

[44] B.J. Goodacre, R.S. Swamidass, J. Lozada, A. Al-Ardah, E. Sahl, A 3D-printed guide for lateral approach sinus grafting: a dental technique, J. Prosthet. Dent 119 (2018) 897–901, https://doi.org/10.1016/j.prosdent.2017.07.014.

[45] Y.K. Hu, Q.Y. Xie, C. Yang, G.Z. Xu, Computer-designed surgical guide template compared with free-hand operation for mesiodens extraction in premaxilla using "trapdoor" method, Medicine (Baltim.) 96 (2017) e7310, https://doi.org/10.1097/MD.0000000000007310.

[46] P. Tack, J. Victor, P. Gemmel, L. Annemans, 3D-printing techniques in a medical setting: a systematic literature review, Biomed. Eng. Online 15 (2016) 115, https://doi.org/10.1186/s12938-016-0236-4.

[47] D. Hoang, D. Perrault, M. Stevanovic, A. Ghiassi, Surgical applications of three-dimensional printing: a review of the current literature & how to get started, Ann. Transl. Med. 4 (2016), https://doi.org/10.21037/atm.2016.12.18.

[48] H. Lal, M.K. Patralekh, 3D printing and its applications in orthopaedic trauma: a technological marvel, J Clin Orthop Trauma 9 (2018) 260–268, https://doi.org/10.1016/j.jcot.2018.07.022.
[49] T.D. Crafts, S.E. Ellsperman, T.J. Wannemuehler, T.D. Bellicchi, T.Z. Shipchandler, A.V. Mantravadi, Three-Dimensional printing and its applications in otorhinolaryngology-head and neck surgery, Otolaryngol–Head Neck Surg Off J Am Acad Otolaryngol-Head Neck Surg 156 (2017) 999–1010, https://doi.org/10.1177/0194599816678372.
[50] C.A. Jacobs, A.Y. Lin, A new classification of three-dimensional printing technologies: systematic review of three-dimensional printing for patient-specific craniomaxillofacial surgery, Plast. Reconstr. Surg. 139 (2017) 1211, https://doi.org/10.1097/PRS.0000000000003232.
[51] H.-H. Lin, D. Lonic, L.-J. Lo, 3D printing in orthognathic surgery - a literature review, J Formos Med Assoc Taiwan Yi Zhi 117 (2018) 547–558, https://doi.org/10.1016/j.jfma.2018.01.008.
[52] P. Canzi, M. Magnetto, S. Marconi, P. Morbini, S. Mauramati, F. Aprile, et al., New frontiers and emerging applications of 3D printing in ENT surgery: a systematic review of the literature, Acta Otorhinolaryngol. Ital. 38 (2018) 286–303, https://doi.org/10.14639/0392-100X-1984.
[53] S.M. Roser, S. Ramachandra, H. Blair, W. Grist, G.W. Carlson, A.M. Christensen, et al., The accuracy of virtual surgical planning in free fibula mandibular reconstruction: comparison of planned and final results, J Oral Maxillofac Surg Off J Am Assoc Oral Maxillofac Surg 68 (2010) 2824–2832, https://doi.org/10.1016/j.joms.2010.06.177.
[54] A. Tarsitano, G. Del Corso, L. Ciocca, R. Scotti, C. Marchetti, Mandibular reconstructions using computer-aided design/computer-aided manufacturing: a systematic review of a defect-based reconstructive algorithm, J Cranio-Maxillo-Fac Surg Off Publ Eur Assoc Cranio-Maxillo-Fac Surg 43 (2015) 1785–1791, https://doi.org/10.1016/j.jcms.2015.08.006.
[55] T. Numajiri, H. Nakamura, Y. Sowa, K. Nishino, Low-cost design and manufacturing of surgical guides for mandibular reconstruction using a fibula, Plast Reconstr Surg Glob Open 4 (2016) e805, https://doi.org/10.1097/GOX.0000000000000682.
[56] A.K. Schneider, J.W. Pierrepont, G. Hawdon, S. McMahon, Clinical accuracy of a patient-specific femoral osteotomy guide in minimally-invasive posterior hip arthroplasty, Hip Int J Clin Exp Res Hip Pathol Ther 28 (2018) 636–641, https://doi.org/10.1177/1120700018755691.
[57] J. Pierrepont, W. Riddell, B. Miles, J. Baré, A. Shimmin, Clinical accuracy of a patient-specific guide for delivering a planned femoral neck osteotomy, Orthop Proc 98-B (2016), https://doi.org/10.1302/1358-992X.98BSUPP_9.ISTA2015-131, 131–131.
[58] J. Arnal-Burró, R. Pérez-Mañanes, E. Gallo-Del-Valle, C. Igualada-Blazquez, M. Cuervas-Mons, J. Vaquero-Martín, Three dimensional-printed patient-specific cutting guides for femoral varization osteotomy: do it yourself, The Knee 24 (2017) 1359–1368, https://doi.org/10.1016/j.knee.2017.04.016.
[59] J. Shi, W. Lv, Y. Wang, B. Ma, W. Cui, Z. Liu, et al., Three dimensional patient-specific printed cutting guides for closing-wedge distal femoral osteotomy, Int. Orthop. (2018), https://doi.org/10.1007/s00264-018-4043-3.
[60] R. Pérez-Mañanes, J.A. Burró, J.R. Manaute, F.C. Rodriguez, J.V. Martín, 3D surgical printing cutting guides for open-wedge high tibial osteotomy: do it yourself, J. Knee Surg. 29 (2016) 690–695, https://doi.org/10.1055/s-0036-1572412.
[61] G.G. Jones, M. Jaere, S. Clarke, J. Cobb, 3D printing and high tibial osteotomy, EFORT Open Rev 3 (2018) 254–259, https://doi.org/10.1302/2058-5241.3.170075.
[62] S. Omori, T. Murase, K. Oka, Y. Kawanishi, K. Oura, H. Tanaka, et al., Postoperative accuracy analysis of three-dimensional corrective osteotomy for cubitus varus deformity with a custom-made surgical guide based on computer simulation, J. Shoulder Elb. Surg. 24 (2015) 242–249, https://doi.org/10.1016/j.jse.2014.08.020.
[63] H. Hoekstra, W. Rosseels, A. Sermon, S. Nijs, Corrective limb osteotomy using patient specific 3D-printed guides: a technical note, Injury 47 (2016) 2375–2380, https://doi.org/10.1016/j.injury.2016.07.021.
[64] L. Mattei, P. Pellegrino, M. Calò, A. Bistolfi, F. Castoldi, Patient specific instrumentation in total knee arthroplasty: a state of the art, Ann. Transl. Med. 4 (2016), https://doi.org/10.21037/atm.2016.03.33.
[65] E. Thienpont, P.-E. Schwab, P. Fennema, Efficacy of patient-specific instruments in total knee arthroplasty: a systematic review and meta-analysis, J Bone Joint Surg Am 99 (2017) 521–530, https://doi.org/10.2106/JBJS.16.00496.
[66] B.M. Holzapfel, H. Pilge, P.M. Prodinger, A. Toepfer, S. Mayer-Wagner, D. W. Hutmacher, et al., Customised osteotomy guides and endoprosthetic reconstruction for periacetabular tumours, Int. Orthop. 38 (2014) 1435–1442, https://doi.org/10.1007/s00264-014-2314-1.
[67] W.G. Blakeney, R. Day, L. Cusick, R.L.C. Smith, Custom osteotomy guides for resection of a pelvic chondrosarcoma, Acta Orthop. 85 (2014) 438–441, https://doi.org/10.3109/17453674.2014.920988.
[68] F. Gouin, L. Paul, G.A. Odri, O. Cartiaux, Computer-assisted planning and patient-specific instruments for bone tumor resection within the pelvis: a series of 11 patients, Sarcoma (2014), https://doi.org/10.1155/2014/842709.
[69] L. Ma, Y. Zhou, Y. Zhu, Z. Lin, Y. Wang, Y. Zhang, et al., 3D-printed guiding templates for improved osteosarcoma resection, Sci. Rep. 6 (2016) 23335, https://doi.org/10.1038/srep23335.
[70] F. Wang, J. Zhu, X. Peng, J. Su, The application of 3D printed surgical guides in resection and reconstruction of malignant bone tumor, Oncol Lett 14 (2017) 4581–4584, https://doi.org/10.3892/ol.2017.6749.